RSC Advances

PAPER

View Article Online
View Journal | View Issue

Cite this: *RSC Adv.*, 2017, **7**, 13325

Growth of Zr/N-codoped TiO_2 nanorod arrays for enhanced photovoltaic performance of perovskite solar cells

Zhenlong Zhang,[a] Junfeng Li,[a] Xiaoli Wang,[a] Jianqing Qin,[a] Wenjia Shi,[a] Yuefeng Liu,[a] Huiping Gao[a] and Yanli Mao*[ab]

Received 26th December 2016
Accepted 22nd February 2017

DOI: 10.1039/c6ra28669k

rsc.li/rsc-advances

In this paper, Zr and N co-doped TiO_2 (Zr/N–TiO_2) nanorod arrays were synthesized using a hydrothermal method and perovskite solar cells were fabricated using them as an electron transfer layer. The solar cells based on Zr/N–TiO_2 presented an enhanced performance compared with those based on un-doped TiO_2. The solar cell performance was optimized by changing the Zr doping content. The efficiency of solar cells based on Zr/N–TiO_2 with a Zr doping content of 1% (Zr/Ti, atomic ratio) has been achieved at 12.6%, which was 31.6% higher than that of solar cells based on un-doped TiO_2. To get an insight into the enhancement, some investigations were carried out. The results indicate that the larger open voltage (V_{oc}) could be due to the larger conduction band offset resulting from the smaller energy band gap for Zr/N–TiO_2, and the enlarged short current (I_{sc}) could be attributed to the faster electron transfer and reduced recombination rate for Zr/N–TiO_2 NRs. These induce the enhancement of solar cell efficiency.

1. Introduction

Recently, perovskite solar cells (PSCs) have attracted more attention due to their high efficiency, low cost, and long charge diffusion length.[1–4] The power conversion efficiency (PCE) of perovskite solar cells has increased to over 22% (ref. 5) within a very short period of time. Typically, mesoporous PSCs are composed of three layers, the electron transfer material (ETM) layer, the perovskite material layer, and the hole transfer material (HTM) layer. TiO_2 has been widely utilized as an ETM in PSCs due to its chemical inertness, photostability, non-toxicity and low cost production.[6,7] However, the wide band gap (3.2 eV) and rapid recombination rate of photogenerated carriers limit the applications of TiO_2.

One of the strategies to reduce the recombination rate of photogenerated carriers is element doping of TiO_2. It has been reported that metal element doping, such as Mg–TiO_2,[8] Cd–TiO_2,[9] Zr–TiO_2,[10] W–TiO_2,[11] *etc.*, and nonmetal doping, such as F–TiO_2,[12] can effectively improve the performance of electron transfer layer in PSCs. Recently, theoretical calculations and experimental data have demonstrated that the recombination rate of photogenerated carriers in TiO_2 can be further reduced by metal and nonmetal co-doping, such as Zr/N co-doping.[13–16] The Zr/N co-doping TiO_2 could enhance the energy conversion efficiency of dye-sensitized solar cells (DSSCs), narrow the band gap, and improve the absorption in visible light range.[16] However, there are no reports on the applications of Zr/N co-doping TiO_2 in perovskite solar cells until now.

In our previous paper,[17] we investigated the effect of doping N content on the performance of perovskite solar cells, in which the solar cells with the doping N content of 1% (N/Ti, nominal atomic ratio) presented the best performance. Based on the previous work, in the present study, we synthesized Zr and N co-doped TiO_2 (Zr/N–TiO_2) nanorod arrays and fabricated the perovskite solar cells using them as electron transfer layer. The solar cell performance was optimized by changing the Zr doping contents. The PCE of solar cells based on Zr/N–TiO_2 with the Zr doping content of 1% (Zr/Ti, nominal atomic ratio) has been achieved 12.6%, which was 31.6% higher than that of solar cells based on un-doped TiO_2. The possible mechanisms of the enhancement were investigated.

2. Experimental

2.1 Growth of TiO_2 nanorod arrays

FTO-coated glass substrate was patterned by etching with Zn metal powder and 2 M HCl diluted in deionized water, and cleaned by sonication for 20 min in detergent, acetone, 2-propanol, and ethanol, respectively. Oxygen plasma was subsequently used to treat the substrate for 20 min. A compact layer of TiO_2 was formed on FTO by treating the substrate in a 0.2 M aqueous solution of $TiCl_4$ at 70 °C for 30 min. TiO_2 nanorods (NRs) were grown on the compact layer by a hydrothermal method.[18] In brief, 20 mL of 37% hydrochloric acid and 20 mL of deionized water were mixed. Subsequently 0.7 mL of

[a]*School of Physics and Electronics, Henan University, Kaifeng 475004, China. E-mail: ylmao1@163.com; Tel: +86-371-23893703*

[b]*Institute for Computational Materials Science, Henan University, Kaifeng 475004, China*

titanium(IV) *n*-butoxide (99%, Aladdin reagent) was added and stirred for 30 min. In the next step, nothing was added to the solution for the growth of un-doped TiO_2, a certain amount of $CO(NH_2)_2$ (N/Ti, nominal atomic ratio, 1%) was added for the growth of N doped TiO_2 (N–TiO_2), and pre-calculated amount of $CO(NH_2)_2$ (N/Ti, nominal atomic ratio, 1%) and $Zr(NO_3)_4 \cdot 5H_2O$ (Zr/Ti, nominal atomic ratio, 0.5%, 1%, 3%, and 5%) were added for the growth of Zr/N codoped TiO_2 (Zr/N–TiO_2). The mixed solution and a compact layer coated FTO substrate was sealed in a stainless steel autoclave. The sealed autoclave was placed inside the oven preheated to 170 °C for several hours. After cooling down to room temperature, the TiO_2 nanorods film was rinsed with ethanol and deionized water, and annealed at 500 °C for 60 min.

2.2 Materials preparation

Methylammonium iodide (CH_3NH_3I) was synthesized using a previously reported method.[19] Typically, aqueous solution of hydroiodic acid (HI) (5 mL, 57 wt% in water, Aladdin Reagent) was reacted with methylamine (CH_3NH_2) (12 mL, 33 wt% in absolute ethanol, Aladdin reagent) at 0 °C for 2 h with constant stirring under nitrogen atmosphere. Methylammonium iodide was crystallized by removing the solvent with a rotary evaporator. The generated white powder was washed with diethyl ether for three times and dried in vacuum for overnight at 60 °C. The perovskite precursor solution was prepared by dissolving CH_3NH_3I and lead(II) chloride ($PbCl_2$) in anhydrous *N*,*N*-dimethylformamide (DMF) at a 3 : 1 molar ratio at 60 °C.

2.3 Solar cell fabrication

The perovskite precursor solution was spin-coated on the annealed TiO_2 film at 2000 rpm for 60 s in an argon-filled glove box. The sample was dried on a hotplate at 110 °C for 60 min. The hole-transporter layer was deposited by spincoating a solution of 2,2′,7,7′-tetrakis(*N*,*N*-di-*p*-methoxyphenyl-amine)9,9′-spirobifluorene (spiro-MeOTAD) at 2000 rpm for 60 s. The spiro-MeOTAD solution was prepared by dissolving 72.3 mg of spiro-MeOTAD in 1 mL of chlorobenzene, to which 28.8 μL of 4-*tert*-butylpyridine and 17.5 μL of lithium bis(trifluoromethanesulfonyl) imide (Li-TFSI) solution (520 mg Li-TSFI in 1 mL acetonitrile, Aladdin reagent) were added. Finally, a gold layer with a thickness of 80 nm was thermally evaporated on top of the device.

2.4 Characterization

X-ray diffraction (XRD) patterns were recorded on a DX-2700 diffractometer with Cu Kα radiation with $\lambda = 0.1542$ nm. Photocurrent–voltage (*I*–*V*) measurements were performed using a Keithley 2440 Sourcemeter under AM 1.5 G illumination from a Newport Oriel Solar Simulator with an intensity of 100 mW cm^{-2}. The active area was 0.1 cm^2 determined by a shadow mask. Morphologies and microstructures were observed with a scanning electron microscope (SEM, JEM-7001F, JEOL) equipped with an energy dispersive spectrometer (EDS). UV-vis absorption spectra were collected on a UV-vis spectrophotometer (Varian Cary 5000). Steady-state photoluminescence (PL) and time-resolved photoluminescence (TRPL) measurements were acquired with a FLS 980 E fluorometer (Edinburgh Photonics), with an excitation source of 515 nm diode laser. The electrochemical impedance spectroscopy (EIS) was performed under a forward bias of 0.6 V under 1 sun illumination conditions with an electrochemical workstation (CHI660e, Shanghai CHI Co., Ltd.) with the frequency range from 1 Hz to 300 kHz. The magnitude of the alternative signal was 10 mV.

3. Results and discussion

We synthesized un-doped, N doped, and Zr/N co-doped TiO_2 nanorod arrays, and fabricated perovskite solar cells using them as an electron transfer material. *I*–*V* measurements were performed by reverse scan (RS) and forward scan (FS). The photovoltaic parameters were obtained by the average of RS and FS for each device. The short current (I_{sc}), open voltage (V_{oc}), fill factor (FF), and power conversion efficiency (PCE) of the solar cells were obtained by an average of the data from 20 pieces of devices. Fig. 1A shows the dependence of PCE on Zr doping contents. It displays that the PCE of solar cells is the maximum at the Zr doping content of 1% (Zr/Ti, nominal atomic ratio). There is an optimal doping content for Zr incorporation. When the content of Zr was lower than its optimal level, the Zr impurity energy level would be a separation center, which could improve the separation of photoinduced carriers. In contrast,

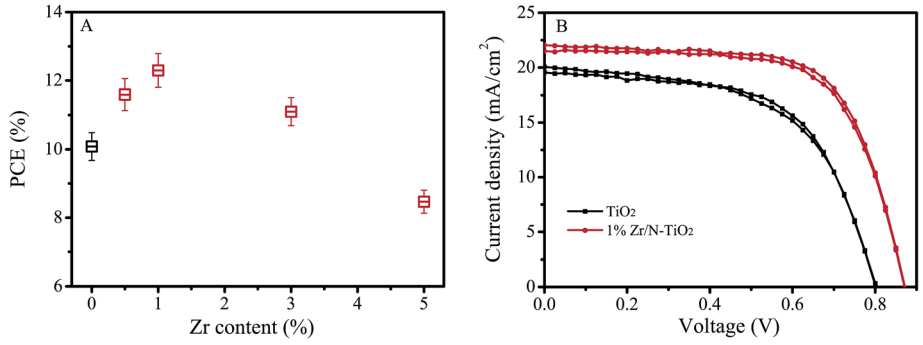

Fig. 1 (A) Dependence of solar cells PCE on Zr doping contents. (B) *I*–*V* curves of best performance solar cells based on un-doped TiO_2 and 1% Zr/N–TiO_2 NRs.

Table 1 Photovoltaic parameters of the solar cells based on un-doped TiO_2, 1% N–TiO_2, and 1% Zr/N–TiO_2 NRs

Sample	V_{oc} (V)	J_{sc} (mA cm^{-2})	FF	PCE (%)
TiO_2	0.80 ± 0.02	19.2 ± 0.6	0.62 ± 0.03	9.5 ± 0.3
1% N–TiO_2	0.82 ± 0.01	20.5 ± 0.7	0.65 ± 0.02	10.9 ± 0.2
1% Zr/N–TiO_2	0.88 ± 0.03	21.6 ± 0.7	0.66 ± 0.02	12.5 ± 0.1

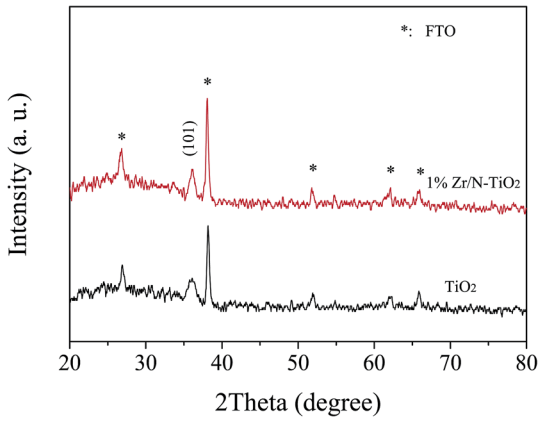

Fig. 2 XRD patterns of un-doped TiO_2 and 1% Zr/N–TiO_2 NRs.

when the content of Zr was higher than its optimal level, Zr impurity energy level would be a recombination center, which could increase the recombination of photoinduced carriers.[14,20]

Table 1 shows the photovoltaic parameters of the solar cells based on un-doped TiO_2, 1% N–TiO_2, and 1% Zr/N–TiO_2 NRs. The photovoltaic parameters of solar cells on 1% Zr/N–TiO_2 NRs are enhanced compared with those of solar cells on un-doped TiO_2 and 1% N–TiO_2 NRs. The high PCE of 12.6% has been obtained for the solar cells on 1% Zr/N–TiO_2 NRs, which is 31.6% higher than that of solar cells on un-doped TiO_2 NRs. Fig. 1B shows the *I–V* curves of best performance solar cells based on un-doped TiO_2 and 1% Zr/N–TiO_2 NRs.

To explain the enhancement phenomenon, we carried out some investigations. Fig. 2 shows the XRD patterns of un-doped TiO_2 and 1% Zr/N–TiO_2 NRs. The peaks labelled with stars were assigned to SnO_2 (JCPDS card, 41-1445) on FTO substrate. The diffraction peak at 36.1° is assigned to the (101) planes of rutile TiO_2 (JCPDS card, 21-1276).[21] Only one peak appears in the XRD patterns, which suggests that almost all the crystallites grew preferentially along the (101) plane parallel to the substrate surface.[22] For the XRD patterns of Zr/N–TiO_2 NRs, Zr peaks did not observed, which might be due to the homogeneous distribution of Zr with Ti in the samples[23] and small amount of Zr doping contents.

Fig. 3 shows the XPS spectra of 1% Zr/N–TiO_2 NRs. The peaks located at 458.5 and 464.3 eV in Fig. 3a are corresponding to Ti $2p_{3/2}$ and Ti $2p_{1/2}$, respectively.[24,25] The binding energy at 529.8 eV in Fig. 3b is attributed to the O 1s.[24,25] The peak at 400.1 eV in Fig. 3c is ascribed to the N 1s.[24,25] The peaks at 182.1 and 184.5 eV in Fig. 3d are assigned to the Zr $3d_{5/2}$ and Zr $3d_{3/2}$, respectively.[24] The XPS spectra demonstrated that both Zr and N atoms are doped into the TiO_2 samples.

Fig. 4A and B show the plane-view SEM images of un-doped TiO_2 and 1% Zr/N–TiO_2 NRs, respectively. Fig. 4C and D show the cross sectional SEM images of un-doped TiO_2 and 1% Zr/N–

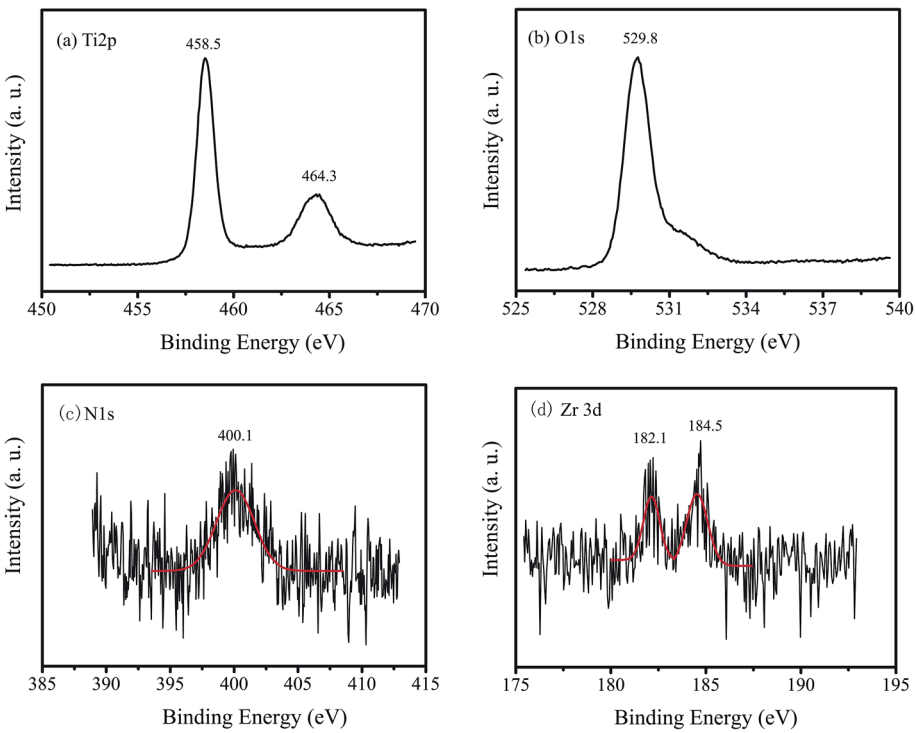

Fig. 3 XPS spectra of 1% Zr/N–TiO_2 NRs. (a) Ti 2p, (b) O 1s, (c) N 1s, and (d) Zr 3d.

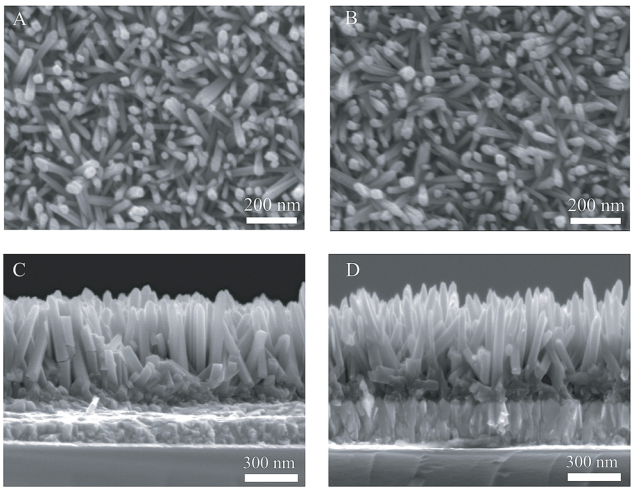

Fig. 4 SEM images of un-doped TiO_2 (A and C), and 1% Zr/N–TiO_2 (B and D).

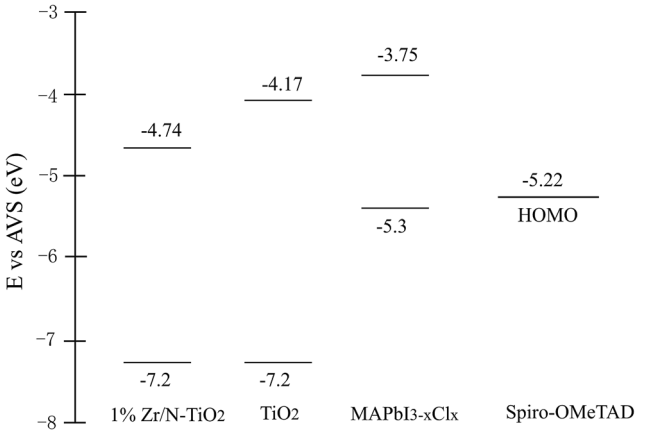

Fig. 6 Energy band diagrams of TiO_2, $MAPbI_{3-x}Cl_x$, and spiro-OMeTAD.

TiO_2 NRs, respectively. The diameter and length of the un-doped TiO_2 NRs were determined to be 50 ± 5 nm and 480 ± 15 nm, respectively. The diameter and length of the 1% Zr/N–TiO_2 NRs were determined to be 40 ± 8 nm and 460 ± 35 nm, respectively. The diameter of N–TiO_2 NRs is slightly decreased compared with that of un-doped TiO_2 NRs. The length distribution of 1% Zr/N–TiO_2 NRs is more ununiform than that of un-doped TiO_2 NRs. This could be attributed to the effect of Zr/N doping.

Fig. 5A shows the UV-vis absorption spectra of un-doped TiO_2 and 1% Zr/N–TiO_2 NRs. The Zr/N–TiO_2 NRs presented a stronger absorption intensity than un-doped TiO_2. The energy band gap (E_g) can be determined using the Tauc plot which is shown below,[26]

$$(\alpha h\nu)^{1/2} = A(h\nu - E_g) \quad (1)$$

where α, ν, A, and E_g are the optical absorption coefficient, frequency, proportionally constant, and energy band gap, respectively. The Tauc curve is shown in Fig. 5B, from which energy band gap (E_g) can be determined to be 3.03 and 2.63 eV for un-doped TiO_2 and 1% Zr/N–TiO_2 NRs, respectively. With the doping of Zr atom, the energy band gap of TiO_2 NRs becomes smaller. This is in accordance with the previous report,[13] which demonstrated that N/Zr-co-doped TiO_2 narrowed the band gap, brought the N 2p gap states closer to the valence band, and enhanced lifetimes of photoexcited carriers with density functional theory (DFT) calculations. According to the energy band gaps calculated from Fig. 5 and the previous report,[27] the energy band diagrams of TiO_2, $MAPbI_{3-x}Cl_x$, and spiro-OMeTAD are schematically shown in Fig. 6. The conduction band offset between 1% Zr/N–TiO_2 and $MAPbI_{3-x}Cl_x$ is the larger than that between un-doped TiO_2 and $MAPbI_{3-x}Cl_x$ due to its narrow energy band gap, which might be one of the reasons to present a higher voltage for Zr/N–TiO_2 based solar cells.[28]

Photoluminescence (PL) can provide an evidence of electron extraction and transfer efficiency.[29,30] Therefore we measured the PL spectra of un-doped TiO_2/$MAPbI_{3-x}Cl_x$ and 1% Zr/N–TiO_2/$MAPbI_{3-x}Cl_x$ and shown in Fig. 7A. The peak at 780 nm is attributed to the emission from $MAPbI_{3-x}Cl_x$.[1] The PL intensity of Zr/N–TiO_2/$MAPbI_{3-x}Cl_x$ is weaker than that of un-doped TiO_2/$MAPbI_{3-x}Cl_x$, which demonstrated that the efficiency of electron extraction and transport of Zr/N–TiO_2/$MAPbI_{3-x}Cl_x$ is more than that of un-doped TiO_2/$MAPbI_{3-x}Cl_x$.

Fig. 7B displays the time-resolved photoluminescence (TRPL) kinetic decay curves of un-doped TiO_2/$MAPbI_{3-x}Cl_x$ and 1% Zr/N–TiO_2/$MAPbI_{3-x}Cl_x$. The TRPL curve was fitted to a biexponential function,

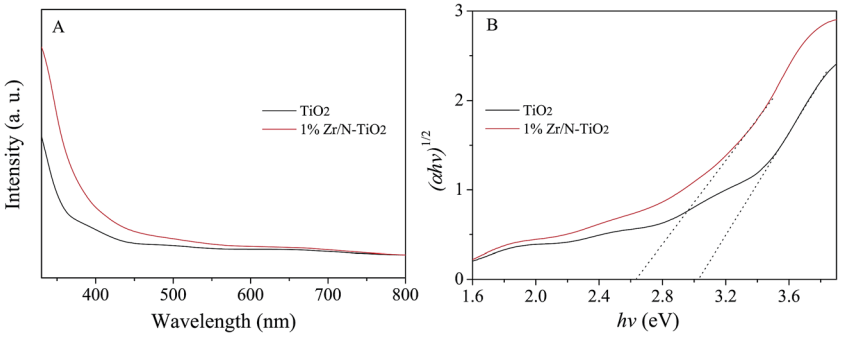

Fig. 5 (A) UV-vis absorption spectra of un-doped TiO_2 and 1% Zr/N–TiO_2 NRs. (B) Tauc curves.

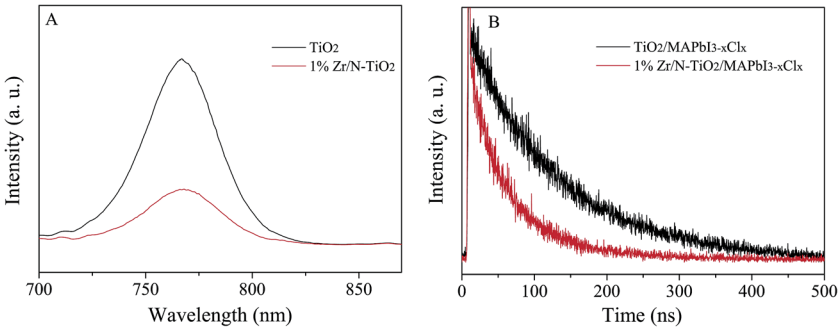

Fig. 7 (A) PL, and (B) TRPL spectra of un-doped TiO_2/$MAPbI_{3-x}Cl_x$ and 1% Zr/N–TiO_2/$MAPbI_{3-x}Cl_x$.

Table 2 Parameters of the TRPL spectra

Sample	τ_1/ns	% of τ_1	τ_2/ns	% of τ_2
TiO_2/$MAPbI_{3-x}Cl_x$	55.1	31.3	121.4	67.7
1% Zr/N–TiO_2/$MAPbI_{3-x}Cl_x$	28.5	43.3	95.2	56.7

$$I(t) = A_1 \exp\left(\frac{t}{\tau_1}\right) A_2 + \exp\left(\frac{t}{\tau_2}\right) \quad (2)$$

The detailed parameters are summarized in Table 2. The fast decay (τ_1) might be originated from the transportation of free carriers from perovskite layer to the respective hole or electron contact. The slow decay (τ_2) could be attributed to the radiative recombination of free charge carriers before the charge collection.[31,32] From Table 2, we can see that the fast decay time (28.5 ns) and slow decay time (95.2 ns) of Zr/N–TiO_2/$MAPbI_{3-x}Cl_x$ are less than those of un-doped TiO_2/$MAPbI_{3-x}Cl_x$ (55.1 ns and 121.4 ns), while the fraction of fast decay process (31.3% and 43.3%) was increased. This proves the improved electron extraction and transport efficiency, and reduced charge recombination of Zr/N–TiO_2 contrast to un-doped TiO_2.

Table 3 Fitting parameters of EIS date

Sample	R_s/Ω	R_{co}/Ω	R_{rec}/Ω	CPE-T/F
TiO_2	34.8	59.3	12.7	6.3×10^{-6}
1% Zr/N–TiO_2	17.4	22.2	83.1	4.8×10^{-5}

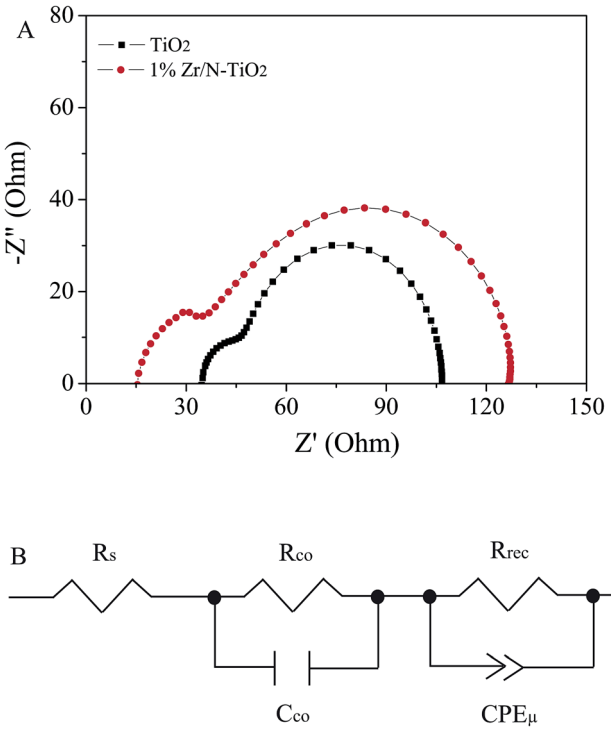

Fig. 8 (A) EIS spectra of solar cells that based on un-doped TiO_2 and 1% Zr/N–TiO_2 NRs based solar cells. (B) Equivalent circuit for fitting the EIS data.

Electrochemical impedance spectroscopy (EIS) is a powerful technique to reveal the underlying carrier transport behavior in perovskite solar cells.[33,34] The Nyquist plots of solar cells based on un-doped TiO_2 and 1% Zr/N–TiO_2 NRs are shown in Fig. 8A, in which two RC arcs were observed. The data were fitted to an equivalent circuit shown in Fig. 8B. The high-frequency RC element is attributed to contact resistance (R_{co}) at the interfaces, while the low-frequency element is ascribed to the recombination resistance (R_{rec}) and chemical capacitance (C_μ) of the system, and the R_s is an additional contribution from series resistance.[18,35] The fitting parameters are listed in Table 3. The total series resistance ($R_s + R_{co}$) for the cells based on Zr/N–TiO_2 is smaller than that on un-doped TiO_2, while the recombination resistance of the former is larger than that of the latter, which indicates that an enhanced charge transport ability and induced carrier recombination rate for the cells based on Zr/N–TiO_2. This agrees well with the *I–V* measurements.

4. Conclusion

In this study, Zr/N-codoped TiO_2 NRs were synthesized and perovskite solar cells based on them were fabricated. The solar cells based on Zr/N–TiO_2 NRs presented an enhanced performance compared with those on un-doped TiO_2 NRs. The solar cell performance was optimized by changing the Zr doping contents. The PCE of solar cells based on Zr/N–TiO_2 with the Zr doping content of 1% (Zr/Ti, atomic ratio) has been achieved 12.6%, which was 31.6% higher than that of solar cells based on

un-doped TiO_2. To explain the enhancement, some investigations were performed. EDS and Tauc plot spectra indicated the incorporation of Zr in TiO_2 nanorods. Absorption spectra showed higher absorption of visible light for Zr/N–TiO_2 than un-doped TiO_2. The Zr doping reduced the energy band gap from 3.03 to 2.64 eV. The PL and TRPL spectra displayed the faster electron transfer from perovskite layer to Zr/N–TiO_2 than to un-doped TiO_2. EIS showed the smaller resistance of device based on Zr/N–TiO_2 than that on un-doped TiO_2.

Acknowledgements

This work is supported by the NSFC-Henan Province Joint Fund (U1604144), Science Fund of Henan Province (162300410020), National Science Research Project of Education Department of Henan Province (No. 17A140005), Science and Technology Development Project of Henan Province (No. 142102210389).

References

1 N. Ahn, D. Y. Son, I. H. Jang, S. M. Kang, M. Choi and N. G. Park, *J. Am. Chem. Soc.*, 2015, **137**, 8696–8699.
2 D. P. McMeekin, G. Sadoughi, W. Rehman, G. E. Eperon, M. Saliba, M. T. Horantner, A. Haghighirad, N. Sakai, L. Korte, B. Rech, M. B. Johnston, L. M. Herz and H. J. Snaith, *Science*, 2016, **351**, 151–155.
3 H. Tsai, W. Y. Nie, J. C. Blancon, C. C. Toumpos, R. Asadpour, B. Harutyunyan, A. J. Neukirch, R. Verduzco, J. J. Crochet, S. Tretiak, L. Pedesseau, J. Even, M. A. Alam, G. V. Gupta, J. Lou, P. M. Ajayan, M. J. Bedzyk, M. G. Kanatzidis and A. D. Mohite, *Nature*, 2016, **536**, 312–316.
4 S. Michael, M. Taisuke, D. Konrad, J. Y. Seo, A. Ummadisingu, S. M. Zakeeruddin, J. P. Correa-Baena, W. R. Tress, A. Abate, A. Hagfeldt and M. Gratzel, *Science*, 2016, **354**, 206–209.
5 National Renewable Energy Laboratory Best Research-Cell Efficiencies, https://www.nrel.gov/ncpv/images/efficiency_chart.jpg, accessed 17 May 2016.
6 K. Mahmood, B. S. Swain, A. R. Kirmani and A. Amassian, *J. Mater. Chem. A*, 2015, **17**, 9051–9057.
7 J. H. Heo, S. H. Im, J. H. Noh, T. N. Mandal, C. S. Lim, J. A. Chang, Y. H. Lee, H. J. Kim, A. Sarkar, M. K. Nazeeruddin, M. Gratzel and S. I. Seok, *Nat. Photonics*, 2013, **7**, 487–492.
8 K. Manseki, T. Ikeya, A. Tamura, T. Ban, T. Sugiura and T. Yoshida, *RSC Adv.*, 2014, **4**, 9652–9655.
9 Y. M. Li, Y. Guo and X. F. Zhou, *Electrochim. Acta*, 2016, **200**, 29–36.
10 H. Nagaoka, F. Ma, D. W. deQuilettes, S. M. Vorpahl, M. S. Glaz, A. E. Colbert, M. E. Ziffer and D. S. Ginger, *J. Phys. Chem. Lett.*, 2015, **6**, 669–675.
11 J. W. Liu, J. Zhang, G. Q. Yue, X. W. Lu, Z. Y. Hu and Y. J. Zhu, *Electrochim. Acta*, 2016, **195**, 143–149.
12 X. Q. Zhang, Y. P. Wu, Y. Huang, Z. H. Zhou and S. Shen, *J. Alloys Compd.*, 2016, **681**, 191–196.
13 X. J. Yao, X. D. Wang, L. Su, H. Yan and M. Yao, *J. Mol. J. Mol. Catal. A: Chem.*, 2011, **351**, 11–16.
14 R. Dhabbe, A. Kadam, P. Korake, M. Kokate, P. Waghmare and K. Garadkar, *J. Mater. Sci.*, 2015, **26**, 554–563.
15 M. Zhang, X. L. Yu, D. D. Lu and J. J. Yang, *Nanoscale Res. Lett.*, 2013, **8**, 543–551.
16 J. Y. Park, K. H. Lee, B. S. Kim, C. S. Kim, S. E. Lee, K. Okuyama, H. D. Jang and T. O. Kim, *RSC Adv.*, 2014, **4**, 9946–9953.
17 Z. L. Zhang, J. F. Li, X. L. Wang, J. Q. Qin, W. J. Shi, Y. F. Liu, H. P. Gao and Y. L. Mao, *Nanoscale Res. Lett.*, 2017, **12**, 43–49.
18 J. F. Li, Z. L. Zhang, H. P. Gao, Y. Zhang and Y. L. Mao, *J. Mater. Chem. A*, 2015, **3**, 19476–19482.
19 M. M. Lee, J. Teuscher, T. Miyasaka, T. N. Murakami and H. J. Snaith, *Science*, 2012, **338**, 643–647.
20 P. Goswami and J. N. Gangul, *Dalton Trans.*, 2013, **42**, 14480–14490.
21 H. S. Kim, J. W. Lee, N. Yantara, P. P. Boix, S. A. Kulkarni, S. Mhaisalkar, M. Gratzel and N. G. Park, *Nano Lett.*, 2013, **13**, 2412–2417.
22 F. Zhang and X. H. Liu, *Thin Solid Films*, 1998, **326**, 171–174.
23 K. V. Buneesh, D. K. Kim and D. W. Park, *Nanoscale*, 2010, **2**, 1222–1228.
24 C. Feng, Y. Wang, J. Zhang, L. Yu, D. Li, J. Yang and Z. Zhang, *Appl. Catal., B*, 2012, **113**, 61–71.
25 M. Zhang, X. L. Yu, D. D. Lu and J. J. Yang, *Nanoscale Res. Lett.*, 2013, **8**, 543–550.
26 X. Y. Liu, H. W. Zheng, Z. L. Zhang, X. S. Liu, R. Q. Wan and W. F. Zhang, *J. Mater. Chem.*, 2011, **21**, 4108–4116.
27 H. S. Kim and N. G. Park, *J. Phys. Chem. Lett.*, 2014, **5**, 2927–2934.
28 Y. L. Li, W. H. Sun, W. B. Yan, S. Y. Ye, H. T. Peng, Z. W. Liu, Z. Q. Bian and C. H. Huang, *Adv. Funct. Mater.*, 2015, **25**, 4867–4873.
29 P. S. Archana, A. Gupta, M. M. Yusoff and R. Jose, *Appl. Phys. Lett.*, 2014, **105**, 53901.
30 Y. Shi, K. Wang, Y. Du, H. Zhang, J. Gu, C. Zhu, L. Wang, W. Guo, A. Hagfeldt, N. Wang and T. Ma, *Adv. Mater.*, 2013, **25**, 4413–4419.
31 H. H. Wang, Q. Chen, H. Zhou, L. Song, S. Luo, Z. S. Louis, N. D. Marco, Y. Fang, P. Sun, T. B. Song, H. Chen and Y. Yang, *J. Mater. Chem. A*, 2015, **3**, 9108–9115.
32 D. Zhong, B. Cai, X. L. Wang, Z. Yang, Y. D. Xing, S. Miaoa, W. H. Zhang and C. Li, *Nano Energy*, 2015, **11**, 409–418.
33 A. Dualeh, T. Moehl, N. Tetreault, J. Teuscher, P. Gao, M. K. Nazeeruddin and M. Gratzel, *ACS Nano*, 2013, **8**, 362–373.
34 V. Gonzalez-Pedro, E. J. Juarez-Perez, W.-S. Arsyad, E. M. Barea, F. Fabregat-Santiago, I. Mora-Sero and J. Bisquert, *Nano Lett.*, 2014, **14**, 888–893.
35 D. Y. Liu, J. L. Yang and T. L. Kelly, *J. Am. Chem. Soc.*, 2014, **136**, 17116–17122.

